Inorganic Chemistry

pubs.acs.org/IC Article

High-Pressure Synthesis and Structure of Quasi-One-Dimensional Ba_3MSe_5 (M = Ti, Zr, and Hf)

Zelong Wang,[#] Guodong Wang,[#] Wenmin Li,[#] Zhe Wang, Runteng Chen, Lei Duan, Jianfa Zhao, Zheng Deng, Jianfeng Zhang,* Tingjiang Yan,* Jun Zhang,* Xiancheng Wang, and Changqing Jin*

Cite This: *Inorg. Chem.* 2025, 64, 13705−13714 Read Online

ACCESS | Metrics & More | Article Recommendations | Supporting Information

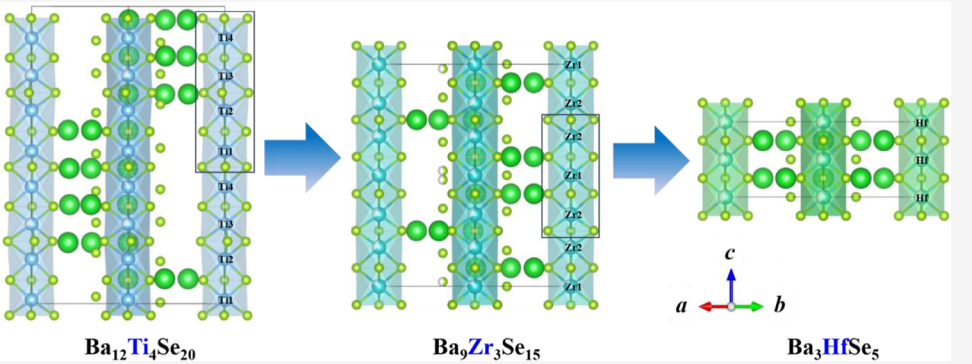

ABSTRACT: The ternary selenides Ba_3MSe_5 (M = Ti, Zr, and Hf) were successfully synthesized through a solid-state reaction under high-pressure and high-temperature conditions. These compounds crystallize in a hexagonal structure, consisting mainly of one-dimensional (1D) face-sharing MSe_6 octahedral chains and Se chains. The intriguing superlattice along 1D chains was identified by theoretically calculating the Fermi surface and phonon spectrum of the Ba_3MSe_5 primitive cell (where M = Ti, Zr, and Hf). These superlattices exhibit average tetramerization, trimerization, and the primitive structures, respectively, as the M metal ions change from the 3d to 5d period. For the Ti- and Zr-containing compounds, the *c*-axis lengths are four times and three times that of the primitive structure, respectively. The space groups of $P31c$, $P\bar{6}c2$, and $P6_3/mcm$ were compatible with the Ti, Zr, and Hf selenides, respectively, resulting in the lattice parameters of a = 9.5304(8) Å and c = 25.3505(3) Å for $Ba_{12}Ti_4Se_{20}$, a = 9.5677(2) Å and c = 19.1731(6) Å for $Ba_9Zr_3Se_{15}$, and a = 9.5756(1) Å and c = 6.3802(7) Å for Ba_3HfSe_5. Comprehensive structural characterizations found that the vacancies on M sites increase from ∼20% to ∼40% and that the electronic hopping between interchains decreases in the Ba_3MSe_5 (M = Ti, Zr, and Hf) system as the M ions evolve from Ti to Hf, which dominates the electronic transport behaviors and results in a gradually increased band gap.

INTRODUCTION

The one-dimensional (1D) material system exhibits many unusual physical phenomena and thereby attracts much attention. For example, the quasi-1D conductor $Li_{0.9}Mo_6O_{17}$ undergoes a dimensional crossover from a 1D conductor to 3D metal at ∼24 K, which induces an electronic spin/charge density wave (SDW/CDW) and further leads to a transition to semiconductor.[1] $Rb_2Mo_6Se_6$, consisting of Mo_6Se_6 chains, undergoes a CDW transition at approximately 170 K.[2] Ba_3TiTe_5 exhibits superconductivity under pressure after suppressing the SDW/CDW and non-Fermi liquid behavior in sequence.[3]

There are two types of typical 1D materials with a hexagonal Hf_5Sn_3Cu-anti-type structure. RE_3MX_5 (where RE = rare earth metal, M = Ti, Zr, Hf, Nb, V, Cr, and Mn, and X = P, As, Sb, and Bi)[4−10] and U_3MSb_5 (M = Sc, Ti, Zr, Hf, V, Nb, Cr, and Mn)[11,12] series materials adopt a hexagonal Hf_5Sn_3Cu-anti-type structure with a space group of $P6_3/mcm$ (No. 193). They consist of face-sharing MX_6 octahedral chains and X-chains, which are separated by RE atoms. These 1D MX_6 octahedral chains form a triangular lattice in the *ab* plane, and the X-chains are located at the central sites. The transition metal ions only occupy the (0, 0, 0) site with the equal distance to the neighbors and form uniform 1D chains. Due to the non-negligible contributions of rare earth ions correlating the adjacent 1D MX_6 octahedral chains, these materials exhibit a 3D band structure. For example, the complementary

Received: February 28, 2025
Revised: June 5, 2025
Accepted: June 12, 2025
Published: June 26, 2025

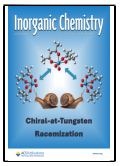

https://doi.org/10.1021/acs.inorgchem.5c00948
Inorg. Chem. 2025, 64, 13705−13714

calculation proves the non-negligible contributions of La to the density of state (DOS) at the Fermi level in La_3MBi_5 and La_3MSb_5 (where M = Ti, Zr, and Hf), and therefore, the La^{3+} ions are not perfectly ionic, leading to a well-defined 3D conductor.[6,13] Diversity in physical properties is also observed. For example, La_3MnAs_5 displays a ferromagnetic metal behavior with a ferromagnetic transition temperature T_c of ∼112 K due to the strong orbital hybridization between the $MnAs_6$ chains and intermediate La atom by the itinerant electrons.[9] La_3CrAs_5 also exhibits a ferromagnetic behavior at ∼50 K owing to a weaker interchain interaction compared with La_3MnAs_5.[8]

Another typical 1D system, $Ba_3M'Ch_5$ (where M′ = Ti, V, Cr, Fe, Co, Nb, Ta, and Sn and Ch = S, Se, and Te),[3,14−24] shows similar crystal structure to RE_3MX_5. The $M'Ch_6$ chains are separated by Ba^{2+}, leading to a weak interchain interaction. These materials are typically synthesized at high-pressure and high-temperature conditions and behave as semiconductors. A variety of structural distortions or superlattices along the 1D MCh_6 chains and M-chains induce many unique physical properties. For example, $Ba_6Cr_2S_{10}$, solved in the *P*-62*c* (No. 190) space group based on the single-crystal measurement, features dimerized CrS_6 chains with antiparallel spin alignment, making $Ba_6Cr_2S_{10}$ a rare ferrotoroidic candidate material.[18] $Ba_9Fe_3Se_{15}$ has a pseudohexagonal structure with a *C*2/*c* space group due to the β angle of 89.9°, as proved by the single-crystal structure analysis. There are two Fe sites in the $FeSe_6$ chain, forming a trimerized superlattice. A tilted screw spiral magnetic structure breaks the symmetry of space inversion and further causes the electric polarization.[17,25] As mentioned above, the superlattice or subtle structure distortion along 1D chains causes diversified physical properties and, in turn, clarifies the superlattice structure plays the predominant role in elucidating the origin of microphysical behaviors. For instance, a Peierls structural transition revealed in $Rb_2Mo_6Te_6$ and $Cs_2Mo_6Te_6$ can well explain a broad metal−semiconductor transition.[26] However, growing single crystals under high-pressure and high-temperature conditions remains challenging to date. A new method to determine the subtle structural distortions on the 1D chains is always desirable.

As is well-known, Fermi surface nesting often occurs in 1D materials due to the strong electron−phonon coupling. This leads to the formation of CDW and lattice instability, further resulting in structure distortion.[27] The character vector that characterizes the structure change is directly linked to the nesting vector of the 1D Fermi surface. Therefore, it is possible to quantitatively validate the structure stability and distortion degree of a 1D primitive cell by analyzing the phonon spectrum and Fermi surface based on theoretical calculation. In addition, the transport behaviors for the 1D materials are complex and easily disrupted by several factors. For a 1D conducting system, Umklapp scattering has an important influence on the electron transfer along the 1D chains, which usually results in a correlation gap and insulating state.[28,29] Meanwhile, the electronic transport properties in the 1D system are primarily determined by electronic hopping between interchains. In addition, the electron backscattering or disorder induced by the defects in the 1D system tends to localize the electrons, which will further impose the important influences on the transport behavior.[24]

In the present work, quasi-1D Ba_3MSe_5 (M = Ti, Zr, and Hf) materials were synthesized as models to study the superlattice structure and accompanying physical properties evolution when metal ions changed from the 3d to the 5d period. Comprehensive structural and band gap analysis revealed the critical role of disorder induced by the vacancies on the M sites and electronic hopping between interchains in the electronic transport property in the Ba_3MSe_5 system. The diversified superlattice structures within the 1D MSe_6 chain were validated through a combination of theoretical calculations and powder diffraction experiments.

EXPERIMENTAL PART

Ba_3MSe_5 (M = Ti, Zr, and Hf) polycrystalline samples were prepared by high-pressure and high-temperature methods using a 6 × 1400 T cubic anvil high-pressure apparatus. Commercially available lumps of Ba (Alfa, immersed in oil, >99.2% pure) and crystalline powders of Ti (Alfa, 99.99% pure), Zr (Alfa, 99.99% pure), Hf (Alfa, 99.99% pure), and Se (Alfa, 99.999% pure) were used as the starting materials. The precursor BaSe was prepared at 700 °C for 20 h in a vacuum quartz tube. The mixture of BaSe, M (M = Ti, Zr, and Hf), and Se powder with a stoichiometric ratio of 3:1:2 was finely ground and pressed into a cylinder with a diameter of 6 mm and a height of 3 mm, which was then sintered at 1500 °C and 5.5 GPa for 30 min in the cubic high-pressure apparatus. After the high-pressure and high-temperature process, the pure polycrystalline Ba_3MSe_5 (M = Ti, Zr, and Hf) samples were obtained.

The powder X-ray diffraction (XRD) measurements were performed on a Rigaku Smart Lab diffractometer with Cu Kα radiation (λ = 1.54059 Å, 45 kV, and 200 mA) in the 2θ range from 10° to 100° with steps of 0.01°. The Rietveld refinement on the diffraction spectra was conducted with GSAS and EXPGUI packages.[30] Energy-dispersive X-ray (EDX) spectroscopy was measured to confirm the chemical composition of the three compounds Ba_3MSe_5 (M = Ti, Zr, and Hf). The DC magnetic susceptibility was measured using a superconducting quantum interference device (SQUID-VSM; Quantum Design). The electronic transport properties were measured by four-probe electrical conductivity methods using a physical property measurement system (PPMS). The UV−vis diffuse reflectance spectroscopy (DRS) was also used to obtain the band gap.

CALCULATION METHOD

The electron and phonon structures for Ba_3MSe_5 (M = Ti, Zr, and Hf) systems were calculated based on the density functional theory (DFT)[31,32] and density functional perturbation theory (DFPT)[33,34] as implemented in the QUANTUM ESPRESSO (QE) package.[35] The generalized gradient approximation (GGA) of Perdew−Burke−Ernzerhof (PBE) type[36] was chosen for the exchange−correlation functional. The kinetic energy cutoff of the wave function was set to be 80 Ry. In the electronic and 1D phonon structure calculations, we sampled Brillouin zone (BZ) using an 8 × 8 × 10 *k*-point mesh and a 1 × 1 × 6 *q*-point mesh, respectively. The Gaussian smearing method with a width of 0.004 Ry was employed for Fermi surface broadening. In structural optimization, both lattice constants and internal atomic positions were fully relaxed until the forces on all atoms were smaller than 0.002 Ry/Bohr. To map the topography of the Fermi surface and its associated orbital weight information, we utilized the maximally localized Wannier functions[37] interpolation technology. A fine 50 × 50 × 50 *k*/*q*-point mesh was used for

https://doi.org/10.1021/acs.inorgchem.5c00948
Inorg. Chem. 2025, 64, 13705−13714

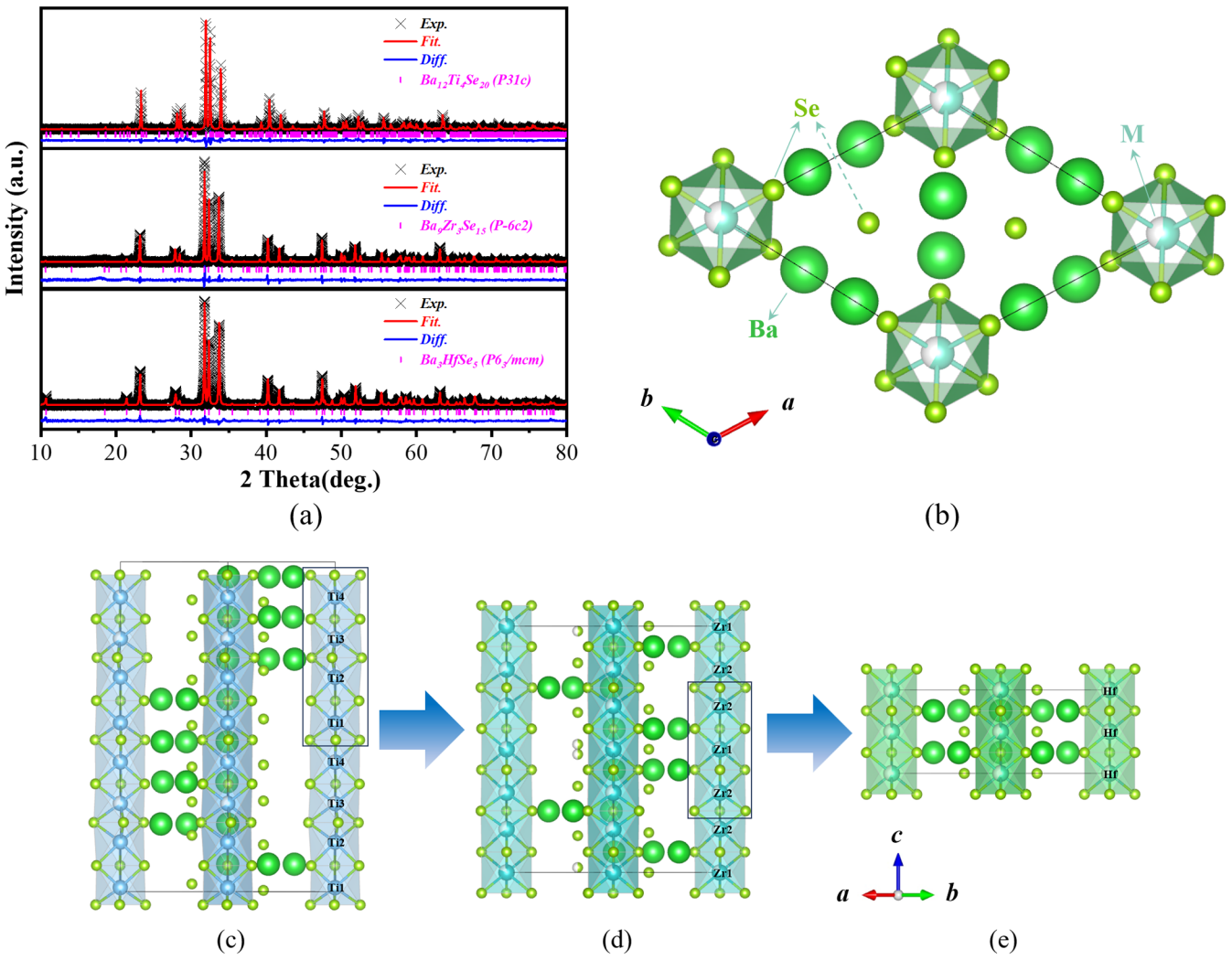

Figure 1. (a) The XRD patterns and the refinement results for the $Ba_{12}Ti_4Se_{20}$, $Ba_9Zr_3Se_{15}$, and Ba_3HfSe_5 samples collected at ambient conditions. (b–e) The crystal structure schemes of Ba_3MSe_5 (M = Ti, Zr, and Hf). (b) shows the [001] projection for the Ba_3MSe_5 material system, and (c–e) is the [110] projection for the crystal structure of $Ba_{12}Ti_4Se_{20}$, $Ba_9Zr_3Se_{15}$, and Ba_3HfSe_5, respectively.

plotting the Fermi surface and calculating the electronic susceptibility.

RESULTS

The powder XRD patterns of as-synthesized Ba_3MSe_5 (M = Ti, Zr, and Hf) samples are shown in Figure 1a, which exhibit similar profiles to the previously discovered quasi-1D "315" system for $(Ba/RE)_3M(X/Ch)_5$ (where X = P, As, Sb, and Bi; M = metal ions; Ch = S, Se, and Te). These structures can be well indexed to the hexagonal structure by powder X powder diffraction analysis software.[38] All three samples primarily consist of face-sharing MSe_6 octahedron chains extending along the *c*-axis, as shown in Figure 1b. Further structural analysis was carried out but could not discern the complex superstructure distortion information within the MSe_6 octahedron chains. For example, Ba_3TiTe_5 is considered to adopt the primitive cell, which agrees with the structures in the RE_3MX_5 system; $Ba_6Cr_2S_{10}$ and $Ba_9Fe_3Se_{15}$ exhibit dimerized and trimerized superstructures along the *c*-axis, respectively, as solved by single-crystal diffraction measurements. Nevertheless, several attempts were made to identify the subgroup according to the hexagonal structure, such as $P\bar{6}c2$ (No. 188) for the trimerization structure, *P*-62*c* (No. 190) for the dimerization, and $P6_3/mcm$ (No. 193) for the primitive cells. And almost indistinguishable results were obtained. Therefore, it is not possible to clarify the accurate structural information along the *c*-axis for the present Ba_3MSe_5 (M = Ti, Zr, and Hf) samples based on the powder diffraction data refinements. We tried to grow single crystals of Ba_3MSe_5 (M = Ti, Zr, and Hf) under high-pressure and high-temperature conditions, including the use of the flux method, but failed. It may originate from the intrinsic structural instability caused by the number of vacancies at metal ion sites. Therefore, a new structural characterization technique is urgently developed.

The detailed theoretical analysis demonstrated the structural distortion along 1D chains in the Ba_3MSe_5 (M = Ti, Zr, and Hf) system, and this will be discussed later. Based on the calculation results, the trimerized structure model and the primitive structure were adopted to refine the powder X-ray diffraction data for $Ba_9Zr_3Se_{15}$ and Ba_3HfSe_5, respectively, using the structures of $Ba_9V_3Te_{15}$[16] and Ba_3TiTe_5[3] as references. For $Ba_{12}Ti_4Se_{20}$, the structure seems more complex. Our theoretical calculations proposed an average tetramerization structure distortion along the 1D direction. Therefore, a tetramerization model with a space group of *P*31*c* was chosen to refine the structure of $Ba_{12}Ti_4Se_{20}$. The XRD patterns and

https://doi.org/10.1021/acs.inorgchem.5c00948
Inorg. Chem. 2025, 64, 13705−13714

Table 1. Crystallographic Data for $Ba_{12}Ti_4Se_{20}$, $Ba_9Zr_3Se_{15}$, and Ba_3HfSe_5 Samples, Including Refinement Parameters, Lattice Constants, and Bond Lengths

$Ba_{12}Ti_4Se_{20}$			
space group	$P31c$		
lattice parameters (Å)	a = 9.5304(8) Å, c = 25.3505(3) Å		
volume (Å^3)	1994.10(1)		
formula weight (g/mol)	6792.63(8)		
density (g/cm^3)	5.65(6)		
refinement parameters	χ^2 = 5.18(3) wRp = 7.36%, Rp = 5.24%		
Ti_1−Se_1 ($x3$) (Å)	2.5852(5)	Ti_2−Se_2 ($x3$) (Å)	2.5995(6)
Ti_1−Se_2 ($x3$) (Å)	2.7640(5)	Ti_2−Se_3 ($x3$) (Å)	3.1328(1)
VBS (Ti_1)	2.7851(7)	VBS (Ti_2)	2.0495(1)
Ti_3−Se_3 ($x3$) (Å)	2.6359(2)	Ti_4−Se_4 ($x3$) (Å)	2.7206(3)
Ti_3−Se_4 ($x3$) (Å)	2.9530(1)	Ti_4−Se_5 ($x3$) (Å)	2.8733(6)
VBS (Ti_3)	2.1397(2)	VBS (Ti_4)	1.9855(3)
Ti_5−Se_5 ($x3$) (Å)	2.8123(2)	Ti_6−Se_6 ($x3$) (Å)	2.7461(4)
Ti_5−Se_6 ($x3$) (Å)	2.5074(3)	Ti_6−Se_7 ($x3$) (Å)	2.6578(4)
VBS (Ti_5)	3.0584(7)	VBS (Ti_6)	2.5309(8)
Ti_7−Se_7 ($x3$) (Å)	2.4352(1)	Ti_8−Se_8 ($x3$) (Å)	2.2826(1)
Ti_7−Se_8 ($x3$) (Å)	2.7794(6)	Ti_8−Se_9 ($x3$) (Å)	3.7867(2)
VBS (Ti_7)	3.6033(6)	VBS (Ti_8)	3.9703(1)
VBS (Ti)	2.76(5)		
occupation of Ti (from XRD refinement)	0.88(3)		
occupation of Ti (from EDX measurement)	0.79(1)		
band gap (eV)	0.34(2)		
$Ba_9Zr_3Se_{15}$			
space group	$P\bar{6}c2$		
lattice parameters (Å)	a = 9.5677(2) Å, c = 19.1731(6) Å		
volume (Å^3)	1519.99(4)		
formula weight (g/mol)	5186.79(5)		
density (g/cm^3)	5.66(6)		
refine parameters	χ^2 = 4.18(1), wRp = 3.11%, Rp = 2.19%		
Zr_1−Se_1 ($x6$) (Å)	2.7557(8)	Zr_2−Se_2 ($x3$) (Å)	2.8651(1)
		Zr_2−Se_3 ($x3$) (Å)	2.7019(6)
VBS (Zr_1)	3.2594(2)	VBS (Zr_2)	3.0976(3)
VBS (Zr)	3.1515(6)		
occupation of Zr_1	0.81(7)		
occupation of Zr_2	0.67(7)		
average occupation (Zr) (from XRD refinement)	0.72(4)		
occupation of Zr (from EDX measurement)	0.70(1)		
band gap (eV)	1.20(2)		
Ba_3HfSe_5			
space group	$P6_3/mcm$		
lattice parameters (Å)	a = 9.5756(1) Å, c = 6.3802(7) Å		
volume (Å^3)	506.64(5)		
formula weight (g/mol)	1818.53(5)		
density (g/cm^3)	5.96(1)		
refine parameters	χ^2 = 6.58(9), wRp = 3.60%, Rp = 2.50%		
Hf−Se ($x6$) (Å)	2.7277(1)		
VBS (Hf)	3.4225(3)		
occupation (Hf) (from XRD refinement)	0.57(4)		
occupation of Hf (from EDX measurement)	0.57(1)		
band gap (eV)	1.60(1)		

the refinement results for Ba_3MSe_5 (M = Ti, Zr, and Hf) samples are shown in Figure 1a. The refinement smoothly converged, and the detailed crystallographic data are summarized in Tables 1 and S1. The lattice parameters are a = 9.5304(8) Å and c = 25.3505(3) Å for $Ba_{12}Ti_4Se_{20}$, a = 9.5677(2) Å and c = 19.1731(6) Å for $Ba_9Zr_3Se_{15}$, and a = 9.5756(1) Å and c = 6.3802(7) Å for Ba_3HfSe_5, respectively. Based on the refinement results, the crystal structure schemes of Ba_3MSe_5 (M = Ti, Zr, and Hf) are plotted in Figure 1b−e, in which the superlattice repeating units in the 1D MSe_6 chains are emphasized by the rectangle. The structures are similar to the hexagonal Hf_5Sn_3Cu-anti-type structure, showing a triangular lattice along the ab plane formed by infinite columns of the face-sharing MSe_6 octahedron. In the middle of the triangle, it is occupied by the Se chains. The distance between the adjacent 1D MSe_6 chains, indicated by the lattice constant a, remains larger than 9.5 Å. Therefore, the Ba_3MSe_5 (M = Ti, Zr, and Hf) samples exhibit well-defined 1D structural characteristics. Our calculation found that the d_{z^2} orbital of the M atoms in 1D MSe_6 chains and the p_z orbital of the Se atoms in the intermediate Se chains contribute to the structural multimerization distortion. Also, it is worth noting that the electronic transport properties of these 1D materials are mainly derived from electron hopping between interchains. Therefore, the increased interchain distance for Ba_3MSe_5 (M = Ti, Zr, and Hf) may contribute to a larger band gap.

The repeating units of superlattice along 1D MSe_6 chains were emphasized by the rectangle shown in Figure 1c,d. There are four Ti atoms forming Ti_1−Ti_2−Ti_3−Ti_4 units in $Ba_{12}Ti_4Se_{20}$, and one Zr_1 located at the (0, 0, 0) site and two Zr_2 at the (0, 0, 0.17612) site form the Zr_2−Zr_1−Zr_2 trimerized units in $Ba_9Zr_3Se_{15}$, while $HfSe_6$ chains solely contain the Hf atom at the (0, 0, 0) site spaced equally with an interatomic distance of 3.1902(1) Å to form uniformly distributed 1D chains along the c-axis. Thus, the coordinated environment of transition metals in Ba_3MSe_5 (M = Ti, Zr, and Hf) samples is different. The bond valence sum (BVS) model relates the bond lengths around a metal center to its oxidation state. The M−Se bond lengths in the three compounds are given in Table 1. According to the formula $V_i = \sum \exp \frac{(R_0 - r_{ij})}{b}$, where V_i is the sum of all valences of a coordination sphere around the metal ion i; r_{ij} is the length of the bond between atoms i and j, respectively; R_0 is the empirically determined distance for a given cation−anion pair; and b is the universal parameter and is set equal to 0.37. For Ti, Zr, and Hf, the R_o values are 2.38, 2.53, and 2.52, respectively. The calculated valence states of M ions (M = Ti, Zr, and Hf) at different sites are shown in Table 1. The average oxidation states for Ti, Zr, and Hf ions in Ba_3MSe_5 (M = Ti, Zr, and Hf) are 2.76(5),

https://doi.org/10.1021/acs.inorgchem.5c00948
Inorg. Chem. 2025, 64, 13705−13714

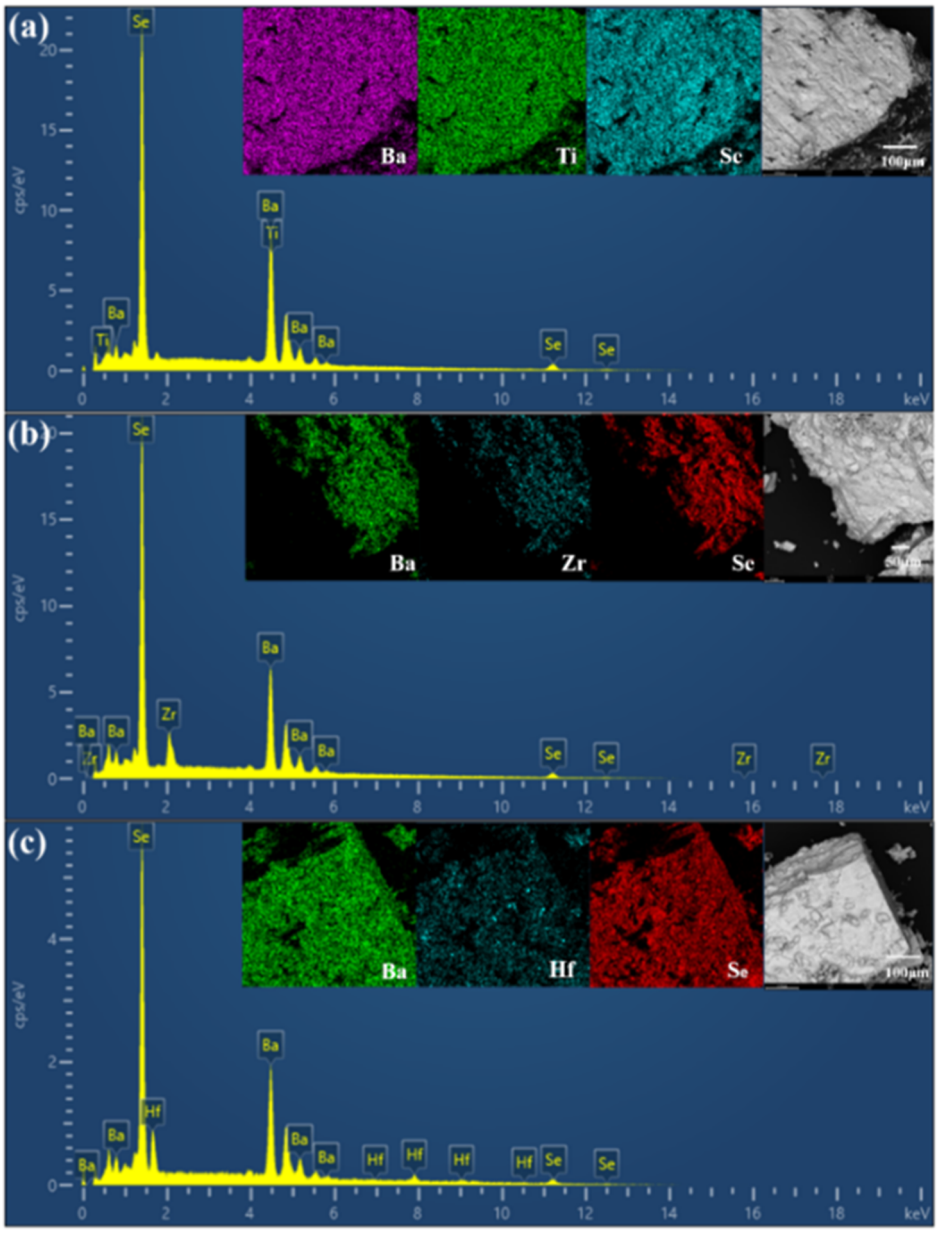

Figure 2. Energy-dispersive X-ray spectrum for the samples of (a) $Ba_{12}Ti_4Se_{20}$, (b) $Ba_9Zr_3Se_{15}$, and (c) Ba_3HfSe_5.

3.15(1), and 3.42(2), exhibiting an increase as the metal evolves from the 3d to the 5d period. These results are supported by our theoretical calculation where charge transfer from the M d_{z^2} orbital to the Se p_z orbital occurs, which is accompanied by the Fermi surface changes from a 1D to 3D character.

Through carefully examining the refined results, the vacancies on the M ion sites are observed for Ba_3MSe_5 (M = Ti, Zr, and Hf) compounds. The average occupations on M sites are 88.3%, 72.4%, and 57.4%, respectively. EDX measurement was performed to determine the chemical composition of the three compounds. In the insets of Figure 2, the morphology and element mapping measurements on the crystalline particles confirmed the uniform distribution of Ba, M, and Se elements in the three samples. The average chemical stoichiometric ratios of Ba:M:Se, obtained by measuring six distinct small particles for the Ti, Zr, and Hf selenides, are 3.00:0.79:4.83, 3.00:0.70:5.10, and 3.00:0.57:4.85, respectively. The experimental results are in good agreement with refinement results, demonstrating the vacancies on M sites in the sample Ba_3MSe_5 (M = Ti, Zr, and Hf). Generally, the distortion of 1D structure to form the superlattice can stabilize the crystal structure, leading to fewer vacancies in these compounds. Therefore, $Ba_{12}Ti_4Se_{20}$ with an average tetramerization structure shows ~20% Ti vacancy, while Ba_3HfSe_5 with a primitive lattice shows Hf vacancy of more than 40%. These vacancies on M sites will exert important influences on the electronic transport property of Ba_3MSe_5 (M = Ti, Zr, and Hf) materials.

Figure 3a shows the temperature dependence of the resistance for the $Ba_{12}Ti_4Se_{20}$ sample. The resistance increases as the temperature decreases, exhibiting semiconducting behavior. The inset presents the linear fit to the curve of $\ln(\rho)$ as a function of inverse temperature using $\rho \propto \exp(\Delta_g/2k_BT)$, where Δ_g is the semiconducting band gap and k_B is the Boltzmann constant. The resistivity curve can be well fitted,

https://doi.org/10.1021/acs.inorgchem.5c00948
Inorg. Chem. 2025, 64, 13705−13714

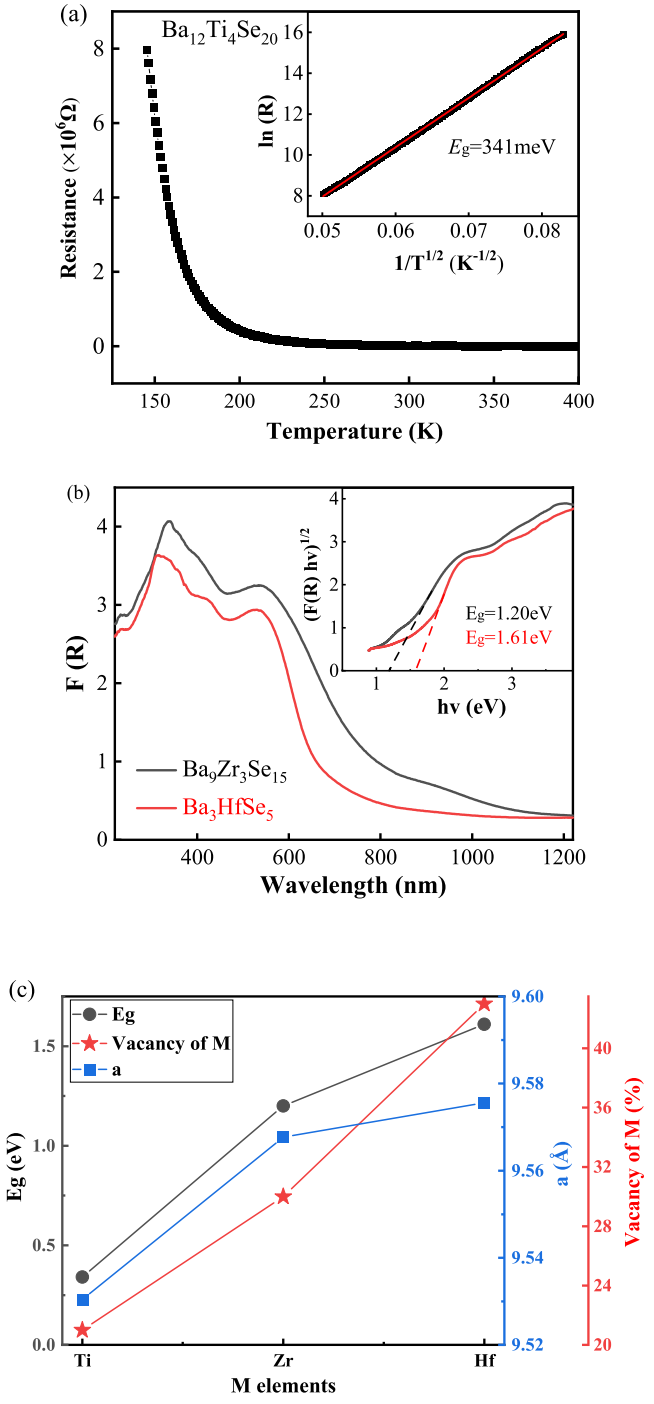

Figure 3. (a) The resistance as a function of temperature for the $Ba_{12}Ti_4Se_{20}$ sample, and the inset shows the inversed temperature dependence of ln(ρ); (b) UV−vis DRS spectra of $Ba_9Zr_3Se_{15}$ and Ba_3HfSe_5; (c) the changes of the band gap, lattice constant a and vacancies on the M sites in the Ba_3MSe_5 (M = Ti, Zr, and Hf) sample as the metal ions evolve from Ti to Hf.

and the band gap Δ_g of $Ba_{12}Ti_4Se_{20}$ is estimated to be 0.34 eV. For $Ba_9Zr_3Se_{15}$ and Ba_3HfSe_5, the band gaps were determined by UV−vis diffuse reflectance spectroscopy due to resistances that were too large for electronic transport measurement. As shown in Figure 3b, the absorption edge of $Ba_9Zr_3Se_{15}$ shows an obvious red shift compared to that of Ba_3HfSe_5, indicating a decreased band gap. According to the Tauc method, $(\alpha h\nu)^{1/\gamma} = B(h\nu - E_g)$, where α is the energy-dependent absorption coefficient, h is the Planck constant, ν is the photon frequency, E_g is the band gap energy, and B is a constant. The γ factor depends on the nature of the electron transition and is equal to 1/2 or 2 for the direct and indirect transition band gaps, respectively. Based on the assumption that γ equals 2 for the indirect band gap, the band gaps of $Ba_9Zr_3Se_{15}$ and Ba_3HfSe_5 are estimated to be 1.20 and 1.61 eV, respectively. Thus, as shown in Figure 3c, the band gaps exhibit an increase as the compounds evolve from $Ba_{12}Ti_4Se_{20}$ to Ba_3HfSe_5. Magnetic susceptibility measurements revealed that the $Ba_{12}Ti_4Se_{20}$ sample is Pauli paramagnetic, while $Ba_9Zr_3Se_{15}$ and Ba_3HfSe_5 show obvious diamagnetic properties within a measuring temperature range of 2−300 K, as shown in Figure S1 in the Supporting Information. For the Ti, Zr, and Hf, the valence electron configurations are $4s^23d^2$, $5s^24d^2$, and $6s^25d^2$, respectively. The oxidation states of Ti, Zr, and Hf in Ba_3MSe_5 compounds are 2.76(5), 3.15(1), and 3.42(2), respectively. Therefore, valence electrons tend to lose completely as the metal ions evolve from the 3d to the 5d period, which leads to a transition from Pauli paramagnetic to diamagnetic properties for $Ba_{12}Ti_4Se_{20}$, $Ba_9Zr_3Se_{15}$, and Ba_3HfSe_5.

In 1D materials, due to strong electron−phonon coupling, the 1D Fermi surface is prone to nesting, which leads to lattice instability and structural distortion. The nesting vector can quantitatively reflect the characteristics of the structural distortion. By theoretically calculating and analyzing the Fermi surface and phonon spectrum of the Ba_3MSe_5 (M = Ti, Zr, and Hf) primitive cell, it is expected to assess the distortion along the one-dimensional direction, determine the dynamical stability of these materials, and indirectly infer the subtle structural distortions within them.

To study the underlying structure distortion and multimerization, first-principles calculations were carried out on the three systems, Ba_3MSe_5 (where M = Ti, Zr, and Hf). Initially, the calculations were focused on the band structures in their primitive forms. As depicted in Figure 4a−c, each system exhibits two-orbital quasi-1D band dispersions near the Fermi level. These dispersions originate from two distinct orbitals: one is from the d_{z^2} orbital of the M atom and the other from the intermediate Se atomic p_z orbital, as indicated by the orbital weights on the band structure (blue circles represent M d_{z^2} orbitals and red circles represent Se p_z orbitals). The nearly flat Fermi surfaces shown in Figure 5 further confirm the characteristics of the quasi-1D dispersions. Here, the color bar on the right indicates the orbital weights, with blue for M d_{z^2} and red for Se p_z orbitals. As shown in Figure 5, a clear trend observed from M = Ti to Zr to Hf is the reduced occupancy in the Brillouin zone (BZ) of the M d_{z^2} orbitals. This suggests a charge transfer from the M d_{z^2} orbital to the Se p_z orbital, resulting in an increasing valence state of the M atom. In addition to the changes in valence states, it is also found that variations in the Fermi surfaces and Fermi vectors (k_F) play a crucial role in structural multimerization distortion, which will be discussed later.

To investigate the structural stability of these three compounds, phonon calculations were performed along the G-A line of BZ based on the DFPT. As displayed in Figure 6a−c, despite their similar crystal structures, the phonon instabilities of these compounds exhibit significant differences. Specifically, the phonon spectra of Ba_3TiSe_5 and Ba_3ZrSe_5 display two types of imaginary frequencies, which are attributed to the vibrations of M atoms (blue circles) and Se

https://doi.org/10.1021/acs.inorgchem.5c00948
Inorg. Chem. 2025, 64, 13705−13714

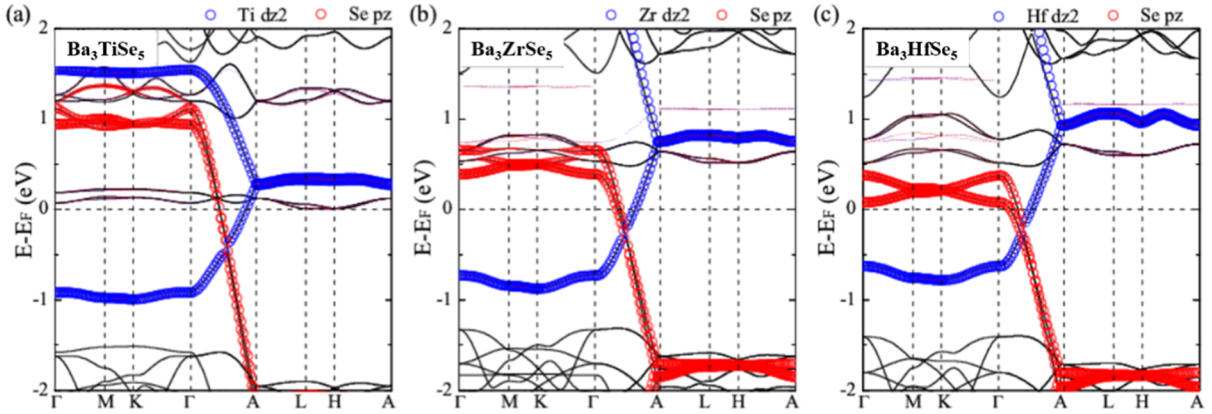

Figure 4. Electronic band structure for the (a) Ba_3TiSe_5, (b) Ba_3ZrSe_5, and (c) Ba_3HfSe_5 systems. The colored circles indicate the projected weights of M d_{z^2} (blue) and Se p_z (red) orbitals.

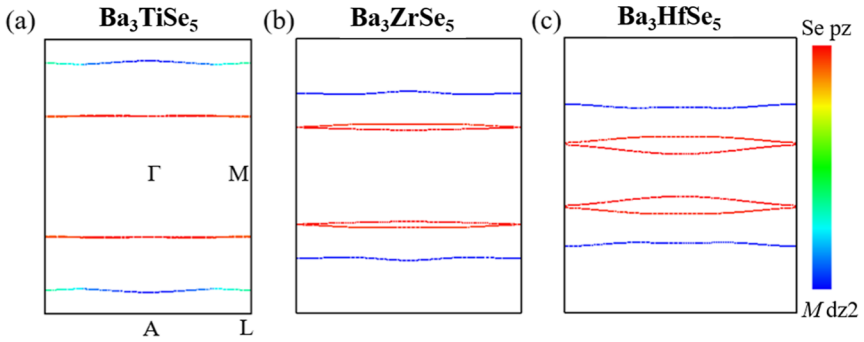

Figure 5. Fermi surfaces of the (a) Ba_3TiSe_5, (b) Ba_3ZrSe_5, and (c) Ba_3HfSe_5 systems. The color bar indicates the orbital weights of the Se p_z orbital (red) and M d_{z^2} orbital (blue).

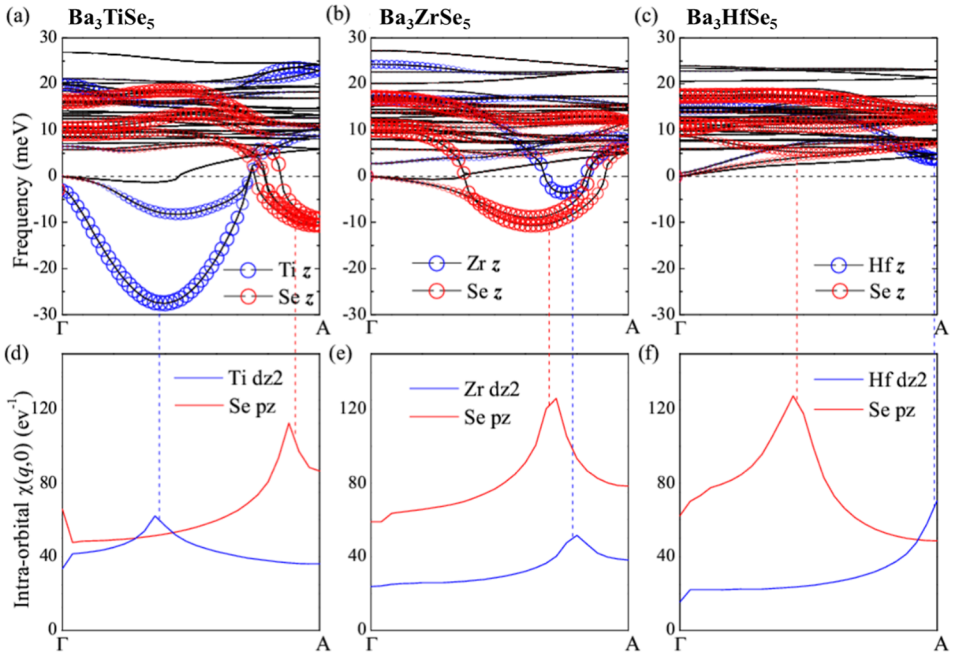

Figure 6. (a–c) The 1D phonon structure along the G-A line of BZ for the (a) Ba_3TiSe_5, (b) Ba_3ZrSe_5, and (c) Ba_3HfSe_5 systems. The colored circles indicate the weights of M (blue) and Se (red) atomic vibrations along the z-direction. (d,e) The intraorbital bare static susceptibility $\chi(q,0)$ within the M atomic d_{z^2} orbital (blue line) and Se atomic p_z orbital (red line). A blue (red) dotted line connects the upper and lower panels, indicating the relationship between the maximum imaginary frequency from M (Se) atoms and the peak of $\chi(q,0)$ within the M d_{z^2} (Se p_z) orbital.

atoms (red circles) in the z-direction. For Ba_3ZrSe_5 in Figure 6b, the characteristic wave vectors exhibiting the highest imaginary frequencies for Zr (0.78π) and Se (0.66π) are close, hinting at a nearly commensurate trimerized structure. In contrast, in the Ba_3TiSe_5 system shown in Figure 6a, the imaginary frequencies for Ti and Se are centered around 0.4π

https://doi.org/10.1021/acs.inorgchem.5c00948
Inorg. Chem. 2025, 64, 13705−13714

and 1.0π, respectively, indicating a more intricate multimerization pattern ranging from two to five. An average tetramerization structure distortion along the 1D direction can be applied in analyzing the X-ray diffraction data. Conversely, Ba_3HfSe_5 exhibits no signs of lattice dynamic instability. It is well-established that the 1D Fermi surface can readily exhibit nesting, potentially leading to lattice instability (or multimerization) via strong electron−phonon coupling such as the Kohn anomaly. For the Ba_3MSe_5 (M = Ti, Zr, and Hf) system, the distinctive phonon instabilities of M and Se atoms are also likely related to the 1D Fermi surface topology and the atomic orbital distribution around the Fermi level. Specifically, the M atomic d_{z^2} orbitals and Se atomic p_z orbitals are more crucial, as their intraorbital scattering mediated by phonons can naturally influence the M/Se atomic structural instabilities in the z-directions. The character vector for the structure multimerization should correspond to the nesting vector. To further investigate the impact of the Fermi surfaces and their nesting effects on phonon instability, we calculated the intraorbital bare static susceptibility, $\chi^{\alpha}(q,0)$, within the M atomic d_{z^2} orbital and the Se atomic p_z orbital:

$$\chi^{\alpha}(q, i\omega) = -\frac{1}{2N}\sum_{mn}\frac{f(\varepsilon_{n,k}) - f(\varepsilon_{m,k+q})}{i\omega + \varepsilon_{n,k} - \varepsilon_{m,k+q}}\langle\alpha|n,k\rangle\langle n, k|\alpha\rangle \langle\alpha|m,k+q\rangle\langle m, k+q|\alpha\rangle$$

where α labels the M d_{z^2} or Se p_z orbital, $f(\varepsilon)$ is the Fermi distribution function, and $\varepsilon_{n,k}$ is the band structure of Figure 4. The calculation results of $\chi^{\alpha}(q,0)$ can be found in Figure 6d−f. Here, we only considered its qz's dependency and integrated the qx and qy subscripts. As illustrated in Figures 6d and 6e, the one-dimensional $\chi(q,0)$ for Ba_3TiSe_5 and Ba_3ZrSe_5 reveal distinct peaks in both the M d_{z^2} (blue line) and Se p_z (red line) orbitals. These peaks correspond with the locations of maximum phonon imaginary frequencies for M and Se atoms in the upper panels, as indicated by the blue and red dotted lines. Meanwhile, for the Ba_3HfSe_5 system, the reduced 1D character of its Fermi surfaces can smear the nesting effect and harden the corresponding phonon modes. Nevertheless, there is still phonon softening around the peaks of χ in Figure 6f. These observations suggest that the Fermi surfaces and the k_F of the M d_{z^2} and Se p_z orbitals significantly influence the periodicity of multimerization in the MSe_3 and Se atomic chains, respectively. Furthermore, the detection effect at the M atomic sites can easily alter the valence states and orbital fillings of the M atoms, thereby modifying their Fermi surfaces and k_F. Consequently, this can effectively impact structural multimerization and band gap.

DISCUSSION

The Ba_3MSe_5 (M = Ti, Zr, and Hf) system, consisting of face-sharing MSe_6 octahedral chains and Se linear chains, both separated by Ba atoms, shows a typical 1D structural character. Compared to the RE_3MX_5 (RE = rare earth metal and U, X = P, As, Sb, and Bi) systems with uniformly distributed MX_6 chains,[4−10] the superlattices in the Ba_3MX_5 (X = S, Se, and Te) systems along the MX_6 octahedral chains exhibit intriguing physical properties, such as pressure-induced superconductivity, spin density wave,[3] and magnetic electronic coupling interaction.[18] The growth of single crystals at high-pressure conditions remains challenging, which leads to difficulties in clarifying the accurate structural distortion of the 1D chains and thereby further exploring the origin of their physical properties. As to the 1D structural character, theoretical calculations in the present work analyzed the 1D Fermi surface, nesting vector, and phonon spectrum of the Ba_3MSe_5 (M = Ti, Zr, and Hf) primitive cell and found that Ba_3MSe_5 (M = Ti and Zr) are stabilized through superlattice distortion. The average tetramerization and trimerization structures for the Ti and Zr counterparts were quantitatively elucidated by characteristic wave vectors, while Ba_3HfSe_5 shows a simple primitive structure with uniformly distributed Hf chains. Thus, by a combination of the powder diffraction data and theoretical calculations, the 1D superlattice character in the Ba_3MSe_5 (M = Ti, Zr, and Hf) system can be well clarified for the 1D system. The currently developed structural analysis methods have some limitations. For instance, when it comes to complex systems, such as $Ba_{12}Ti_4Se_{20}$, these methods may fail to provide accurate structural information. Therefore, the single-crystal structure determination still serves as the most direct evidence, and the presented calculation method can only be regarded as a candidate approach.

The superlattice structure plays a critical role in transport properties of the 1D materials. In the Ba_3MSe_5 (M = Ti, Zr, and Hf) system, more charge transfer from the M d_{z^2} orbital to the Se p_z orbital was observed in the present work, resulting in an increasing valence state of the M ions from Ti to Hf. Meanwhile, the reduced 1D character suppresses the nesting effect and hardens the corresponding phonon modes, which should lead to a 1D conductor in Ba_3HfSe_5. For example, La_3TiBi_5 and La_3TiSb_5 were demonstrated to possess similar electronic structures with 3D Fermi surfaces and exhibit metallic behaviors derived from the La^{3+} ions that are not perfectly ionic.[6,13] In the Ba_3MCh_5 (M = metal and Ch = S, Se, and Te) system, the semiconducting behaviors were revealed by the past research in the Ba_3MCh_5 (M = metal ions and Sn and Ch = S, Se, and Te).[3,15−18,39] First, the 1D conducting behavior can be easily damaged by Umklapp scattering that induces an Umklapp gap, as observed in Ba_3TiTe_5 and also in the present Ba_3HfSe_5. For $Ba_{12}Ti_4Se_{20}$ and $Ba_9Zr_3Se_{15}$, the semiconductor behavior is mainly related to the structure distortion that derives from the nesting of the Fermi surface. In addition, in the 1D material, the electronic hopping between interchains plays the dominant role in the electronic transport property and is closely related to the band gap. The Ba^{2+} ions in the Ba_3MCh_5 system with a larger radius compared to La^{3+} are possibly responsible for the semiconducting behaviors. As shown in Figure 3c, the distance between interchains increases from 9.5304(8) Å for $Ba_{12}Ti_4Se_{20}$, a = 9.5677(2) for $Ba_9Zr_3Se_{15}$ to a = 9.5756(1) for Ba_3HfSe_5 in sequence, which will cause less electron hopping and thereby a larger band gap. In addition, the disorder induced by the vacancy in the 1D system tends to localize the electrons. As mentioned above, the structural distortion stabilizes the crystal structure, resulting in the ∼20% vacancy in $Ba_{12}Ti_4Se_{20}$, while only ∼60% Hf occupancy in Ba_3HfSe_5 was proved. Our experimental results found that the band gap increases and keeps a consistent trend with the quantity of vacancy and interchain's distances in the Ba_3MSe_5 (M = Ti, Zr, and Hf) system, as shown in Figure 3c. Therefore, a conclusion that the vacancy-induced disorder and decreased electronic hopping between interchains together dominate the electronic transport behavior in our synthesized Ba_3MSe_5 (M = Ti, Zr, and Hf) is obtained.

https://doi.org/10.1021/acs.inorgchem.5c00948
Inorg. Chem. 2025, 64, 13705−13714

CONCLUSION

The 1D Ba_3MSe_5 (M = Ti, Zr, and Hf) materials were synthesized for the first time. The superlattice distortion along the 1D chains for the Ba_3MSe_5 (M = Ti, Zr, and Hf) system was identified by combining powder diffraction and theoretical calculation techniques. The detailed structural analysis and band gap measurement revealed the disorder induced by the vacancy on the M sites, and the decreased electronic hopping between interchains in the Ba_3MSe_5 (M = Ti, Zr, and Hf) 1D system may dominate the electronic transport. The character vector of the structural distortion was quantitatively related to the nesting vector in the Fermi surface, characterizing Ti, Zr, and Hf selenides as average tetramerization, trimerization, and the primitive structure, respectively, as the central metal ions M evolve from the 3d to the 5d period. These findings extend the 1D material system and, more importantly, provide an alternative candidate solution for identifying complex 1D superlattices when single-crystal samples are absent. The evolution of physical properties of 1D materials under high pressure is interesting, including 1D−3D structure transition, pressure-induced charge density wave, superconductivity, etc. Further research is in progress.

ASSOCIATED CONTENT

Supporting Information

The Supporting Information is available free of charge at https://pubs.acs.org/doi/10.1021/acs.inorgchem.5c00948.

Additional experimental details and methods, including crystallographic data and magnetic properties of Ba_3MSe_5 (M = Ti, Zr, and Hf) (PDF)

AUTHOR INFORMATION

Corresponding Authors

Jianfeng Zhang − *Center for High Pressure Science & Technology Advanced Research, 100094 Beijing, China;* orcid.org/0000-0001-7922-0839; Email: jianfeng.zhang@hpstar.ac.cn

Tingjiang Yan − *Key Laboratory of Catalytic Conversion and Clean Energy in Universities of Shandong Province, School of Chemistry and Chemical Engineering, Qufu Normal University, Qufu 273165, P. R. China;* orcid.org/0000-0003-1328-3540; Email: tingjiangn@163.com

Jun Zhang − *Beijing National Laboratory for Condensed Matter Physics, Institute of Physics, Chinese Academy of Sciences, Beijing 100190, China; School of Physics, University of Chinese Academy of Sciences, Beijing 100190, China;* orcid.org/0000-0002-9980-9074; Email: zhang@iphy.ac.cn

Changqing Jin − *Beijing National Laboratory for Condensed Matter Physics, Institute of Physics, Chinese Academy of Sciences, Beijing 100190, China; School of Physics, University of Chinese Academy of Sciences, Beijing 100190, China;* Email: jin@iphy.ac.cn

Authors

Zelong Wang − *Key Laboratory of Catalytic Conversion and Clean Energy in Universities of Shandong Province, School of Chemistry and Chemical Engineering, Qufu Normal University, Qufu 273165, P. R. China*

Guodong Wang − *Beijing National Laboratory for Condensed Matter Physics, Institute of Physics, Chinese Academy of Sciences, Beijing 100190, China*

Wenmin Li − *Institute of Quantum Materials and Physics, Henan Academy of Sciences, Zhengzhou 450046, China*

Zhe Wang − *College of Chemistry and Material Science, Hebei Normal University, Shijiazhuang 050024, China*

Runteng Chen − *Beijing National Laboratory for Condensed Matter Physics, Institute of Physics, Chinese Academy of Sciences, Beijing 100190, China*

Lei Duan − *Beijing National Laboratory for Condensed Matter Physics, Institute of Physics, Chinese Academy of Sciences, Beijing 100190, China;* orcid.org/0000-0002-1254-0317

Jianfa Zhao − *Beijing National Laboratory for Condensed Matter Physics, Institute of Physics, Chinese Academy of Sciences, Beijing 100190, China; School of Physics, University of Chinese Academy of Sciences, Beijing 100190, China;* orcid.org/0000-0002-7507-9441

Zheng Deng − *Beijing National Laboratory for Condensed Matter Physics, Institute of Physics, Chinese Academy of Sciences, Beijing 100190, China; School of Physics, University of Chinese Academy of Sciences, Beijing 100190, China*

Xiancheng Wang − *Beijing National Laboratory for Condensed Matter Physics, Institute of Physics, Chinese Academy of Sciences, Beijing 100190, China; School of Physics, University of Chinese Academy of Sciences, Beijing 100190, China;* orcid.org/0000-0001-6263-4963

Complete contact information is available at: https://pubs.acs.org/10.1021/acs.inorgchem.5c00948

Author Contributions

#Z.W., G.W., and W.L. contributed equally to this work.

Notes

The authors declare no competing financial interest.

ACKNOWLEDGMENTS

The present work was supported by the National Key R&D Program of China and the Natural Science Foundation of China under Grants Nos. 12104488, 2023YFA1406001, 2024YFA1408000, and 12474097.

REFERENCES

(1) dos Santos, C. A. M.; White, B. D.; Yu, Y. K.; Neumeier, J. J.; Souza, J. A. Dimensional crossover in the purple bronze $Li_{0.9}Mo_6O_{17}$. *Phys. Rev. Lett.* **2007**, *98* (26), 266405.

(2) Petrović, A. P.; Ansermet, D.; Chernyshov, D.; Hoesch, M.; Salloum, D.; Gougeon, P.; Potel, M.; Boeri, L.; Panagopoulos, C. A disorder-enhanced quasi-one-dimensional superconductor. *Nat. Commun.* **2016**, *7*, 12262.

(3) Zhang, J.; Jia, Y. T.; Wang, X. C.; Li, Z.; Duan, L.; Li, W. M.; Zhao, J. F.; Cao, L. P.; Dai, G. Y.; Deng, Z.; Zhang, S. J.; Feng, S. M.; Yu, R. Z.; Liu, Q. Q.; Hu, J. P.; Zhu, J. L.; Jin, C. Q. A new quasi-one-dimensional compound Ba_3TiTe_5 and superconductivity induced by pressure. *NPG Asia Mater.* **2019**, *11* (1), 60.

(4) Bollore, G.; Ferguson, M. J.; Hushagen, R. W.; Mar, A. New ternary rare-earth transition-metal antimonides RE_3MSb_5 (RE = La, Ce, Pr, Nd, Sm; M = Ti, Zr, Hf, Nb). *Chem. Mater.* **1995**, *7* (12), 2229−2231.

(5) Ferguson, M. J.; Hushagen, R. W.; Mar, A. Crystal structures of La_3ZrSb_5, La_3HfSb_5, and $LaCrSb_3$. Structural relationships in ternary rare-earth antimonides. *J. Alloys Compd.* **1997**, *249* (1−2), 191−198.

(6) Murakami, T.; Yamamoto, T.; Takeiri, F.; Nakano, K.; Kageyama, H. Hypervalent Bismuthides La_3MBi_5 (M = Ti, Zr, Hf) and Related Antimonides: Absence of Superconductivity. *Inorg. Chem.* **2017**, *56* (9), 5041−5045.

(7) Duan, L.; Zhang, J.; Wang, X. C.; Zhao, J. F.; Cao, L. P.; Li, W. M.; Deng, Z.; Yu, R. Z.; Li, Z.; Jin, C. Q. High-pressure synthesis, structure and properties of new ternary pnictides La_3TiX_5 (X = P, As). *J. Alloys Compd.* **2020**, *831*, 154697.
(8) Duan, L.; Wang, X. C.; Zhan, F. Y.; Zhang, J.; Hu, Z. W.; Zhao, J. F.; Li, W. M.; Cao, L. P.; Deng, Z.; Yu, R. Z.; Lin, H. J.; Chen, C. T.; Wang, R.; Jin, C. Q. High-pressure synthesis, crystal structure and physical properties of a new Cr-based arsenide La_3CrAs_5. *Sci. China Mater.* **2020**, *63* (9), 1750−1758.
(9) Duan, L.; Wang, X. C.; Zhang, J.; Hu, Z.; Zhao, J. F.; Feng, Y. G.; Zhang, H. L.; Lin, H. J.; Chen, C. T.; Wu, W.; Li, Z.; Wang, R.; Zhang, J. F.; Xiang, T.; Jin, C. Q. Synthesis, structure, and magnetism in the ferromagnet La_3MnAs_5: Well-separated spin chains coupled via itinerant electrons. *Phys. Rev. B* **2022**, *106* (18), 184405.
(10) Duan, L.; Wang, X. C.; Zhang, J.; Zhao, J. F.; Zhao, Z. W.; Xiao, C.; Guan, C.; Wang, S.; Shi, L.; Zhu, J.; Jin, C. Critical behavior of the ferromagnetic metal La_3CrAs_5 with quasi-one-dimensional spin chains. *J. Alloys Compd.* **2022**, *905*, 164214.
(11) Mar, A.; Tougait, O.; Potel, M.; Noel, H.; Lopes, E. B. Anisotropic transport and magnetic properties of ternary uranium antimonides U_3ScSb_5 and U_3TiSb_5. *Chem. Mater.* **2006**, *18* (18), 4533−4540.
(12) Tkachuk, A. V.; Muirhead, C. P. T.; Mar, A. Structure and physical properties of ternary uranium transition-metal antimonides U_3MSb_5 (M = Zr, Hf, Nb). *J. Alloys Compd.* **2006**, *418* (1−2), 39−44.
(13) Moore, S. H. D.; Deakin, L.; Ferguson, M. J.; Mar, A. Physical properties and bonding in RE_3TiSb_5 (RE = La, Ce, Pr, Nd, Sm). *Chem. Mater.* **2002**, *14* (11), 4867−4873.
(14) Almoussawi, B.; Tomohiri, H.; Kageyama, H.; Kabbour, H. High pressure synthesis of the spin chain sulfide $Ba_9V_3S_{11}(S_2)_2$. *Eur. J. Inorg. Chem.* **2021**, *2021*, 1271−1277.
(15) Zhang, J.; Liu, M.; Wang, X. C.; Zhao, K.; Duan, L.; Li, W.; Zhao, J.; Cao, L. P.; Dai, G. Y.; Deng, Z.; Feng, S.; Zhang, S.; Liu, Q. Q.; Yang, Y. F.; Jin, C. Q. $Ba_9V_3Se_{15}$: a novel compound with spin chains. *J. Phys.: Condens. Matter* **2018**, *30*, 214001.
(16) Zhang, J.; Zhang, X. Y.; Xia, Y. H.; Zhao, J. F.; Duan, L.; Wang, G. D.; Min, B. S.; Cao, H. B.; Dela Cruz, C. R.; Zhao, K.; Sun, H. Y.; Zhu, J. L.; Zhang, J. F.; Xiang, T.; Wang, X. C.; Jin, C. Q. Structure and magnetic properties of $Ba_9V_3Te_{15}$ with ferromagnetic spin chains. *Phys. Rev. B* **2023**, *108* (17), 174423.
(17) Zhang, J.; Komarek, A. C.; Jin, M. L.; Wang, X. C.; Jia, Y. T.; Zhao, J. F.; Li, W. M.; Hu, Z. W.; Peng, W.; Wang, X.; Tjeng, L. H.; Deng, Z.; Yu, R.; Feng, S. M.; Zhang, S. J.; Liu, M.; Yang, Y. F.; Lin, H. J.; Chen, C. T.; Li, X. D.; Zhu, J. L.; Jin, C. Q. High-pressure synthesis, crystal structure, and properties of iron-based spin-chain compound $Ba_9Fe_3Se_{15}$. *Phys. Rev. Mater.* **2021**, *5* (5), 054606.
(18) Zhang, J.; Wang, X. C.; Zhou, L.; Liu, G. X.; Adroja, D. T.; da Silva, I.; Demmel, F.; Khalyavin, D.; Sannigrahi, J.; Nair, H. S.; Duan, L.; Zhao, J. F.; Deng, Z.; Yu, R. Z.; Shen, X.; Yu, R. C.; Zhao, H.; Zhao, J. M.; Long, Y. W.; Hu, Z. W.; Lin, H. J.; Chan, T. S.; Chen, C. T.; Wu, W.; Jin, C. Q. A ferrotoroidic candidate with well-separated spin chains. *Adv. Mater.* **2022**, *34* (12), 2106728.
(19) Jenks, J. M.; Hoggins, J. T.; Rendondiazmiron, L. E.; Cohen, S.; Steinfink, H. Octahedrally Coordinated Iron in Ba-Fe-S system: $Ba_9Fe_3S_{11}(S_2)_2$, a High-Pressure Polymorph of Ba_3FeS_5. *Inorg. Chem.* **1978**, *17* (7), 1773−1775.
(20) Duan, L.; Chen, X.; Wang, Z.; Wei, Y.; Zhang, J.; Feng, Y.; Wang, S.; Du, S.; Zhao, Z.; Xiao, C.; Wang, X.; Jin, C. High-pressure synthesis, structure and physical properties of two quasi-one-dimensional compounds $Ba_9Nb_{2.54}Te_{15}$ and $Ba_9Ta_{1.89}Te_{15}$. *J. Alloys Compd.* **2024**, *1007*, 176496.
(21) Duan, L.; Wang, X. C.; Zhang, J.; Zhao, J. F.; Li, W. M.; Cao, L. P.; Zhao, Z. W.; Xiao, C. J.; Ren, Y.; Wang, S.; Zhu, J. L.; Jin, C. Q. Doping effect on the structure and physical properties of quasi-one-dimensional compounds $Ba_9Co_3(Se_{1-x}S_x)_{15}$ (x = 0 - 0.2). *Chin. Phys. B* **2021**, *30* (10), 106101.
(22) Zhang, J.; Duan, L.; Wang, Z.; Wang, X. C.; Zhao, J. F.; Jin, M. L.; Li, W. M.; Zhang, C. L.; Cao, L. P.; Deng, Z.; Hu, Z. W.; Agrestini, S.; Valvidares, M.; Lin, H. J.; Chen, C. T.; Zhu, J. L.; Jin, C. Q. The synthesis of a quasi-one-dimensional iron-based telluride with antiferromagnetic chains and a spin glass state. *Inorg. Chem.* **2020**, *59* (8), 5377−5385.
(23) Zhang, J.; Jin, M. L.; Li, X.; Wang, X. C.; Zhao, J. F.; Liu, Y.; Duan, L.; Li, W. M.; Cao, L. P.; Chen, B. J.; Wang, L. J.; Sun, F.; Wang, Y. G.; Yang, L. X.; Xiao, Y. M.; Deng, Z.; Feng, S. M.; Jin, C. Q.; Zhu, J. L. Structure-spin-transport anomaly in quasi-1-dimensional $Ba_9Fe_3Te_{15}$ under high pressure. *Chin. Phys. Lett.* **2020**, *37*, 087106.
(24) Zhang, J.; Su, R.; Wang, X. C.; Li, W. M.; Zhao, J. F.; Deng, Z.; Zhang, S. J.; Feng, S. M.; Liu, Q. Q.; Zhao, H. Z.; Guan, P. F.; Jin, C. Q. Synthesis, crystal structures, and electronic properties of one dimensional $Ba_9Sn_3(Te_{1-x}Se_x)_{15}$ (x = 0−1). *Inorg. Chem. Front.* **2017**, *4* (8), 1337−1343.
(25) Zhang, J.; Wang, X.; Hao, Y.; Liu, G.; Zhou, L.; Pajerowski, D. M.; Wang, J.-T.; Zhu, J.; Zhao, J.; Wang, J.; Zhao, Y.; Duan, C.; Long, Y.; Kang, C.-J.; Greenblatt, M.; Jin, C. Ferroelectricity driven by magnetism in quasi-one-dimensional $Ba_9Fe_3Se_{15}$. *arXiv* **2022**, arXiv:2207.10834.
(26) Hor, P. H.; Fan, W. C.; Chou, L. S.; Meng, R. L.; Chu, C. W.; Tarascon, J. M.; Wu, M. K. Study of the metal-semiconductor transition in $Rb_2Mo_6Se_6$, $Rb_2Mo_6Te_6$ and $Cs_2Mo_6Te_6$ under pressures. *Solid State Commun.* **1985**, *55* (3), 231−235.
(27) Johannes, M. D.; Mazin, I. I. Fermi surface nesting and the origin of charge density waves in metals. *Phys. Rev. B* **2008**, *77* (16), 165135.
(28) Giamarchi, T. Umklapp Process and Resistivity in One-Dimensional Fermion Systems. *Phys. Rev. B* **1991**, *44* (7), 2905−2913.
(29) Vescoli, V.; Degiorgi, L.; Henderson, W.; Gruner, C.; Starkey, K. P.; Montgomery, L. K. Dimensionality-driven insulator-to-metal transition in the Bechgaard salts. *Science* **1998**, *281* (5380), 1181−1184.
(30) larson, A. C.; VON Dreele, R. B. *General Structure Analysis System (GSAS)*; Los Alamos National Laboratory Report Laur, 2000; pp 86−748.
(31) Hohenberg, P.; Kohn, W. Inhomogeneous electron gas. *Phys. Rev. B* **1964**, *136* (3b), B864−B871.
(32) Kohn, W.; Sham, L. J. Self-consistent equations including exchange and correlation effects. *Phys. Rev.* **1965**, *140* (4a), A1133−A1138.
(33) Giustino, F. Electron-phonon interactions from first principles. *Rev. Mod. Phys.* **2017**, *89* (1), 015003.
(34) Baroni, S.; de Gironcoli, S.; Dal Corso, A.; Giannozzi, P. Phonons and related crystal properties from density-functional perturbation theory. *Rev. Mod. Phys.* **2001**, *73* (2), 515−562.
(35) Giannozzi, P.; Baroni, S.; Bonini, N.; Calandra, M.; Car, R.; Cavazzoni, C.; Ceresoli, D.; Chiarotti, G. L.; Cococcioni, M.; Dabo, I.; Dal Corso, A.; de Gironcoli, S.; Fabris, S.; Fratesi, G.; Gebauer, R.; Gerstmann, U.; Gougoussis, C.; Kokalj, A.; Lazzeri, M.; Martin-Samos, L.; Marzari, N.; Mauri, F.; Mazzarello, R.; Paolini, S.; Pasquarello, A.; Paulatto, L.; Sbraccia, C.; Scandolo, S.; Sclauzero, G.; Seitsonen, A. P.; Smogunov, A.; Umari, P.; Wentzcovitch, R. M. QUANTUM ESPRESSO: a modular and open-source software project for quantum simulations of materials. *J. Phys.: Condens. Matter* **2009**, *21* (39), 395502.
(36) Perdew, J. P.; Burke, K.; Ernzerhof, M. Generalized gradient approximation made simple. *Phys. Rev. Lett.* **1996**, *77* (18), 3865−3868.
(37) Mostofi, A. A.; Yates, J. R.; Pizzi, G.; Lee, Y. S.; Souza, I.; Vanderbilt, D.; Marzari, N. An updated version of wannier90: A tool for obtaining maximally-localised Wannier functions. *Comput. Phys. Commun.* **2014**, *185* (8), 2309−2310.
(38) Dong, C. Powder X Powder Diffraction Analysis Software (beta version). http://www.ccp14.ac.uk.
(39) Duan, L.; Wang, X. C.; Zhang, J.; Zhao, J. F.; Cao, L. P.; Li, W. M.; Yu, R. Z.; Deng, Z.; Jin, C. Q. Synthesis, structure, and properties of $Ba_9Co_3Se_{15}$ with one-dimensional spin chains. *Chin. Phys. B* **2020**, *29* (3), 036102.

https://doi.org/10.1021/acs.inorgchem.5c00948
Inorg. Chem. 2025, 64, 13705−13714